Analysis of guided resonances in photonic crystal slabs

Shanhui Fan
Department of Electrical Engineering, Stanford University, Stanford, California 94305

J. D. Joannopoulos
Center for Materials Science and Engineering, and Department of Physics, Massachusetts Institute of Technology, Cambridge, Massachusetts 02139

(Received 7 August 2001; revised manuscript received 8 January 2002; published 7 June 2002)

We present a three-dimensional analysis of guided resonances in photonic crystal slab structures that leads to a new understanding of the complex spectral properties of such systems. Specifically, we calculate the dispersion diagrams, the modal patterns, and transmission and reflection spectra of these resonances. From these calculations, a key observation emerges involving the presence of two temporal pathways for transmission and reflection processes. Using this insight, we introduce a general physical model that explains the essential features of complex spectral properties. Finally, we show that the quality factors of these resonances are strongly influenced by the symmetry of the modes and the strength of the index modulation.

DOI: 10.1103/PhysRevB.65.235112 PACS number(s): 42.70.Qs

I. INTRODUCTION

Photonic crystal slabs are a particularly important class of photonic crystal structures. A photonic crystal slab consists of a two-dimensionally periodic index contrast introduced into a high-index guiding layer (Fig. 1). These structures support in-plane *guided modes* that are completely confined by the slab without any coupling to external radiations. These guided modes allow control of light within the layer at the wavelength scale. Therefore, the slab structure may provide the basic substrate for large-scale on-chip integration of photonic components and circuits.[1–8]

In addition to in-plane waveguiding, photonic crystal slabs can also interact with external radiations in complex and interesting ways. Of particular importance here is the presence of *guided resonances* in the structures.[9–15] Similar to the guided mode, a guided resonance also has its electromagnetic power strongly confined within the slab. Unlike the guided mode, however, the resonance can couple to external radiation. Therefore, guided resonances can provide an efficient way to channel light from within the slab to the external environment. This property has been exploited in designs of novel photonic-crystal-based light-emitting diodes,[11,16] lasers,[17,18] and directional output couplers.[19] In addition, the guided resonances can significantly affect the transmission and reflection of externally incident light, resulting in complex resonant line shapes that are useful in filter applications.[9,20]

The purpose of this paper is to present a novel analysis of guided resonances in photonic crystal slabs. Our analysis elucidates a variety of complex spectra phenomena associated with these resonances. We compute the dispersion diagrams and the eigenfield distributions of these resonances with a plane-wave band-structure computation method. We then perform finite-difference time-domain simulations to determine the transmission and reflection spectra and to visualize in real time the interaction between the resonances and incident light. Emerging from these simulations is a key insight that involves the presence of two temporal pathways in the transmission and reflection processes. Based on this insight, we introduce a general and intuitive theory, which uses only interference and energy conservation arguments, to explain all the complex features in the spectral lineshapes. Finally, we analyze the angular and structural dependences of the guided resonances, and we show the wide ranges of tunability in quality factors for these resonances.

II. BAND STRUCTURE OF THE GUIDED RESONANCES

Since the spectral features of the guided resonances in a photonic crystal slab will turn out to depend critically on their modal properties, it is helpful to begin our discussion with a brief overview of the band structure properties of these resonances. Throughout this paper, our model system will consist of a square lattice of air holes introduced into a dielectric slab (Fig. 1). The thickness of the slab is $0.5a$, and the radius of the holes is $0.2a$, where a is the lattice constant. The dielectric constant of slab is 12, which roughly corresponds to the dielectric constant of Si or GaAs at optical wavelengths. For such a structure, because of the translational symmetries within the plane of the slabs, the physical properties of the slabs can be described by a band diagram that relates the frequencies of all the three-dimensional modes to the in-plane wave vectors.[1,2] The band diagram can be computed by a preconditioned conjugate gradient minimization of a Maxwell operator expanded on a plane-wave basis.[21]

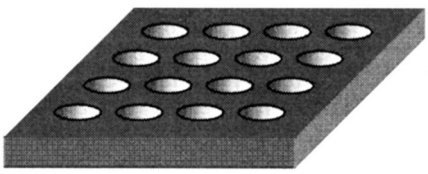

FIG. 1. Photonic crystal slab structure consisting of a square lattice of air holes introduced into a high-index dielectric slab.

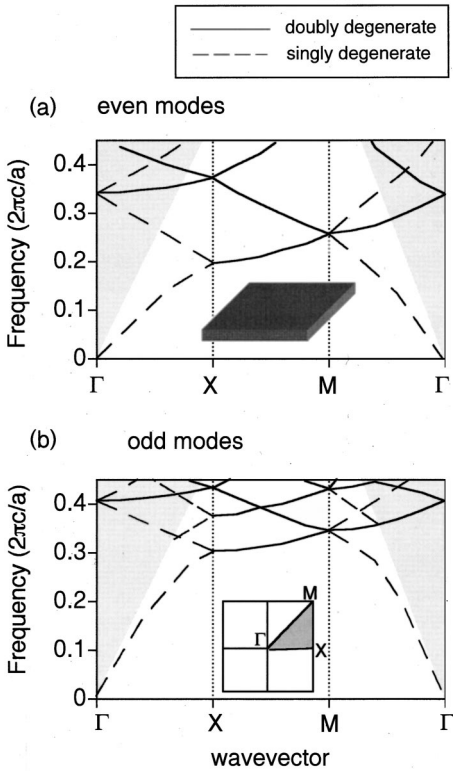

FIG. 2. Band structure for (a) even and (b) odd modes in a uniform dielectric slab. The slab has a thickness of $0.5a$ and a dielectric constant of 12. The band structure is plotted in a reduced-zone scheme, assuming a square lattice with lattice constant a. The even and odd symmetries are defined with respect the mirror plane parallel to the slab. The lines here are the guided modes. The solid lines represent doubly degenerate states, while the dashed lines represent singly degenerate states. The gray regions are the continuum of radiation modes.

To understand the origins of different types of modes in a photonic crystal slab, let us first briefly review the band diagram of a uniform dielectric slab. For this purpose, we consider a uniform slab with a thickness of $0.5a$, and a dielectric constant of 12. The band diagram for this structure is plotted in Fig. 2. Here we exhibit the band diagram using a reduced-zone scheme assuming a square lattice with a lattice constant a. The lines here correspond to the guided modes that are confined within the slab, while the gray region corresponds to the continuum of radiation modes. Radiation modes lie above the *light line*, which is defined as the boundary of the gray region. We separate the guided modes into even or odd modes, characterized with respect to the mirror plane parallel to the slab. The lowest-order even modes have their electric fields parallel to the slab, while the lowest-order odd modes have their magnetic field parallel to the slab. Because of the use of the reduced-zone scheme, some of the guided modes exist above the light line. These modes, however, do not couple to radiation modes because of the underlying continuous translational symmetry of the structure. Also, we note the existence of doubly degenerate bands at many k points and the occurrence of a four fold degeneracy at the Γ point. (The Γ point refers to a zero value of the $\mathbf{k}$ vector parallel to the plane of periodicity.)

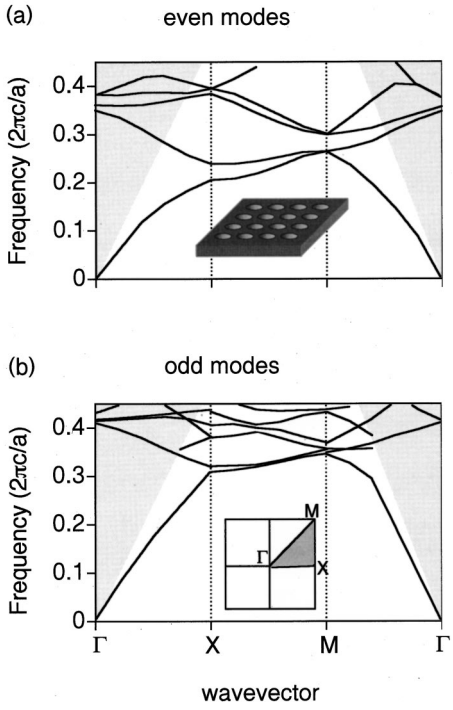

FIG. 3. Band structure for (a) even and (b) odd modes in a photonic crystal slab. The structure is shown in the inset of and consists of a square lattice of air holes with a radius of $0.2a$ introduced into a high-index dielectric slab with a dielectric constant of 12 and a thickness of $0.5a$. (a is the lattice constant.) Even and odd symmetries are defined with respect the mirror plane parallel to the slab. The gray region is the continuum of radiation modes. Solid lines outside the gray region are guided modes. Solid lines within the gray region are guided resonances.

Compared with the band diagram of the uniform dielectric slab, the band diagram of a photonic crystal slab structure displays important similarities and differences. For our model system as shown in Fig. 1, the band diagrams for the even and odd modes are plotted in Figs. 3(a) and 3(b), respectively. Modes below the light line are still *bona fide* guided modes with infinite lifetime, in spite of the large index contrast introduced by the air holes. The guided modes above the light line, on the other hand, can now couple to radiation modes and possess a finite lifetime. These modes therefore become *guided resonances*. They are called ''guided'' since they are closely related to the guided mode bands in a uniform slab and should therefore retain significant portions of the electromagnetic power within the dielectric slab.

The presence of the air holes in the crystal also lowers the translational symmetry of the structure from a continuous one to a discrete one and thereby reduces the degeneracy of the bands. At most k points, (except for the special points Γ, X, and M), the bands are now singly degenerate. At the Γ point, the point group supports a two-dimensional irreducible representation, allowing for the existence of doubly degenerate states. Therefore, the fourfold degeneracy at the Γ point for a uniform slab splits in the presence of the air holes, as clearly seen in Fig. 4, where we plot the frequencies of the resonant modes at Γ as a function of the radius of the holes.

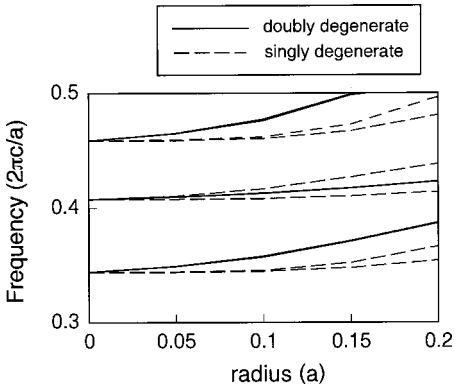

FIG. 4. Frequencies of the resonances at Γ as a function of the radius of the holes in the slab. The slab has a dielectric constant of 12 and a thickness of $0.5a$. The modes are fourfold degenerate in the structure without holes. For structures with holes, the fourfold degeneracy is broken, resulting in a pair of doubly degenerate states and two singly degenerate states.

As the radius of the holes increases, the modes separate into a pair of doubly degenerate states and two singly degenerate states.

For the crystal structure with $r=0.20a$, we show the power density distribution of the first resonant band at Γ in Fig. 5. The mode is singly degenerate with a frequency $\omega=0.35\times 2\pi c/a$. Since any singly degenerate mode should belong to a one-dimensional irreducible representation, the power density distribution of the mode should possess the full symmetry of the lattice. This can be seen in Fig. 5(a), which shows the spatial distribution of the power density on a slice parallel to the slab. Also, the resonant nature of this mode is exhibited in Fig. 5(b), which shows that the power density is strongly confined within the slab.

The band-structure computations thus allow us to examine the dispersion, the field distributions, and the symmetry properties of the guided resonances. For a complete understanding of these resonances, however, we must also study their lifetimes and their interactions with external radiations.

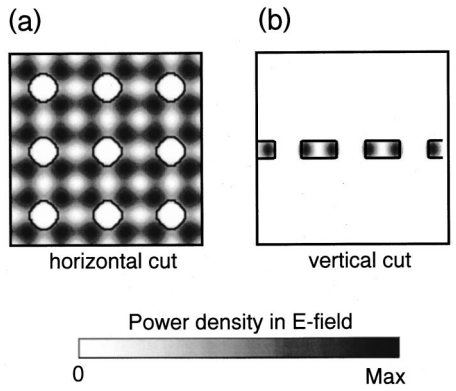

FIG. 5. Spatial distribution of the power density in electric fields on (a) a horizontal slice and (b) a vertical slice for the lowest-order singly degenerate resonance at Γ. The lines indicate the position of the interface between dielectric and air. The white color represents low intensity and the dark color represents high intensity, as indicated by the color bar at the bottom of the figure.

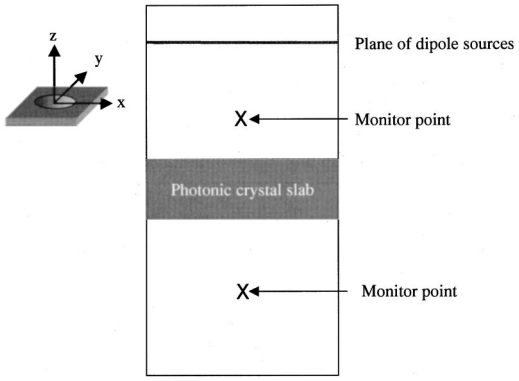

FIG. 6. Cross section of the computational domain for the calculation of transmission and reflection coefficients through a photonic crystal slab. The coordinate system is also shown. The computational domain encloses a single unit cell of the crystal. Bloch boundary conditions are imposed on the four surfaces perpendicular to the slab. The PML absorbing boundary conditions are imposed at the top and bottom surfaces. A plane of dipole sources generates the incident plane waves. The transmitted and reflected amplitudes are determined by recording the fields at the monitor points positioned at both sides of the structure.

These questions will be addressed in the next session by finite-difference time-domain simulations.

III. TIME-DOMAIN ANALYSIS OF THE GUIDED RESONANCES

A. Computational methods

The computational domain for our finite-difference time-domain study[22] is shown in Fig. 6. The domain includes a single unit cell of the crystal. On the top and bottom surfaces of the computational domain, we impose the Perfectly Matched Layer (PML) absorbing boundary conditions.[23] For the remaining four surfaces that are perpendicular to the slab, we impose a Bloch periodic boundary condition on the electric fields **E**:

$$\mathbf{E}(\mathbf{r}+\mathbf{a})=e^{i(\mathbf{k}\cdot\mathbf{a})}\mathbf{E}(\mathbf{r}). \tag{1}$$

Here **a** is a lattice vector of the square lattice and **k** is a wave vector that is parallel to the slab. We note that by Bloch's theorem, **k** is a conserved quantity in the scattering process.

We generate an incident plane wave by placing a source plane consisting of oscillating dipoles near the top surface of the computational domain. For two dipoles in the plane that are separated by a distance vector **r**, we set the relative phase between them to be $e^{i(\mathbf{k}\cdot\mathbf{r})}$. Therefore, in combination with the boundary condition as specified in Eq. (1), the source plane generates an incident plane wave with a parallel wave vector component **k**. In addition, the amplitudes of the dipole moments are set to oscillate at a constant frequency with a Gaussian profile to create a temporal pulse. This computational setup thus allows us to calculate the response functions of the structure at a given **k** for a wide range of frequencies in a single simulation run. (Notice that this is not a constant incidence angle calculation. At a fixed parallel wave vector **k**, the incidence angle changes with frequency.)

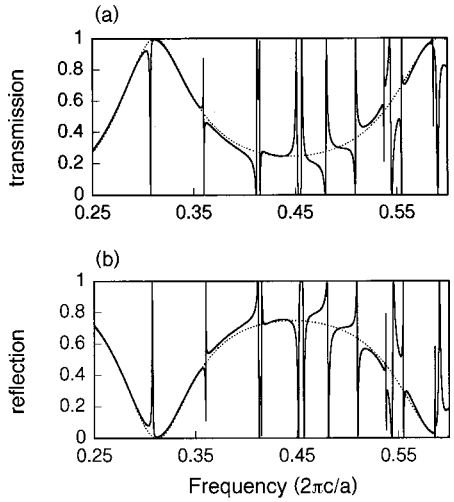

FIG. 7. (a) Transmission and (b) reflection spectra. The solid lines are for the photonic crystal structure shown in Fig. 3(a). The dashed lines are for a uniform dielectric slab with a frequency-dependent dielectric constant, as defined in Eq. (2), and a thickness of $0.5a$. The incident wave is *s* polarized and has a parallel wave vector along the *x* direction $k_x = 0.2 \times 2\pi/a$.

The transmission and reflection spectra are obtained by first Fourier transforming the recorded time sequence of field amplitudes at their respective monitor points. (We note that monitoring the field amplitudes only at the two monitor points is valid for the frequency range $\omega < 2\pi c/a$, where no diffraction occurs.) The spectra are then normalized with respect to the incident pulse, which is calculated in an identical simulation in vacuum without the slab structure. For reflection, the normalization step is preceded by subtracting the incident pulse.

B. Transmission and reflection spectra

Using the computational setup as described in Sec. III 1, we calculate the transmission and reflection coefficients at various *k* points for the structure as shown in Fig. 1. In the case where $\mathbf{k} = \hat{x} \times 0.2 \times 2\pi/a$, the calculated spectra for the *s*-polarized incident wave are shown in Fig. 7. (An *s*-polarized wave has its electric field perpendicular to the plane of incidence. In this case, the electric field is polarized along the *y* direction.) The spectra consist of sharp resonant features superimposed upon a smoothly varying background.

The background in Fig. 7 resembles Fabry-Perot oscillations when light interacts with a uniform dielectric slab. To clearly see this, we fit the background to the spectra of a uniform slab, which are shown as dashed lines in Fig. 7. The uniform slab has the same thickness of $0.5a$ as the crystal, and the light is incident with the same polarization at the same parallel wave vector $\mathbf{k} = \hat{x} \times 0.2 \times 2\pi/a$. The dielectric constant of the uniform slab ε_1, as obtained by the fitting procedure, represents an effective dielectric constant for the photonic crystal. Due to the presence of the holes, such ε_1 is a slowly varying function of the frequency. At low frequencies, the wavelength of incident light is large, and ε_1 for this polarization approaches the average dielectric constant ε_{avg} of the crystal. At higher frequencies, as the incident wave probes more details of the crystal structure, ε_1 starts to deviate from ε_{avg}. Within the frequency range in Fig. 7, i.e., between $0.25 \times 2\pi c/a$ and $0.60 \times 2\pi c/a$, we have found that a frequency-dependent dielectric constant

$$\varepsilon_1(\omega) = -14.16\omega^2 + 15.18\omega + 7.18 \tag{2}$$

gives a very good fit of the background (Fig. 7). The fit here corresponds to varying ε_1 from 10.62 at $\omega = 0.25 \times 2\pi c/a$ to 11.5 at $\omega = 0.60 \times 2\pi c/a$. (As a comparison, the average dielectric constant for the crystal is 10.6.) Therefore, except for the sharp resonance features, the background of the spectra for the crystal can be adequately accounted for using the model of a uniform dielectric slab with a frequency-dependent dielectric function.

C. Line shape analysis

Superimposed upon the smooth background in the spectra for the crystals are sharp resonant features. Such features come from the guided resonances of the slab. In most cases, the line shapes for these resonances are asymmetric and rather complicated. Extensive experimental and theoretical work has been performed for guided resonances in structures with one-dimensionally periodic index variation.[24–31] For structures with two-dimensional periodicity, these resonances have also been studied numerically using the rigorous coupled-wave analysis (RCWA) method[20] and, analytically, using vector coupled-mode theory.[13,15] Here we would like to present a novel analysis from a time-domain perspective. We will observe important features in the time-domain signatures of the resonances. And based upon the observation, we will introduce a general and intuitive model to account for the underlying physics.

The transmission and reflection spectra are related to the time-varying fields by a Fourier transformation. It is therefore informative to examine the time dependence of the fields. As an example, we show in Fig. 8(a) the electric field amplitude at the transmission monitor point as a function of time steps for the calculation that gives the spectra shown in Fig. 7. The time sequence consists of two distinct stages: an initial pulse and a tail of long decay.

The presence of these two stages indicates the existence of two pathways in the transmission processes. The first pathway is a direct transmission process, where a portion of the incident energy goes straight through the slab and generates the initial pulse. The Fourier transformation of the initial pulse should account for the background in the transmission spectra. The second pathway is an indirect transmission process, where the remaining portion of the incident energy excites the guided resonances. The power in the resonances then decays slowly out of the structure and produces the long decaying tail. By Fourier transforming the decaying tail, we obtain the typical symmetric Lorentzian line shapes, as shown in Fig. 8(b). The analysis of the resonant line shape thus allows us to determine the quality factor *Q* of the resonance. [The quality factor *Q* is defined as $\omega/(\delta\omega)$, where ω is the center frequency and $\delta\omega$ is the resonant linewidth.] A few examples of the *Q* values for this structure are 360 for

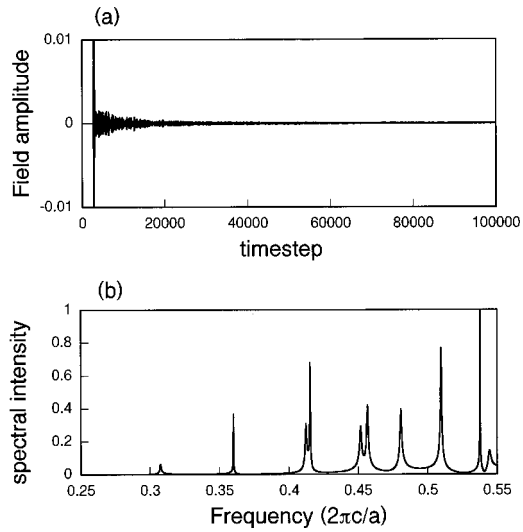

FIG. 8. (a) Field amplitude at the monitor point as a function of time step for the same calculation as shown in Fig. 7. Notice the existence of two separate stages: an initial pulse and a long decaying tail. (b) Fourier transformation of the amplitude as shown in (a) from time step 20 000–100 000. The spectral intensity exhibits Lorentzian line shapes.

the resonance at $\omega=0.31(2\pi c/a)$ and 2500 for the resonance at $\omega=0.36(2\pi c/a)$. The transmission property, therefore, is determined by the interference between the direct and the indirect pathways. The same observation can be made for the reflected amplitude as well. In solid-state and atomic physics, similar interference phenomena are commonly referred to as the Fano resonances.[32] Such a temporal interference phenomenon has also been analyzed previously for surface plasmons in metallic thin films.[33]

Taking into consideration the interference between these two pathways, we can construct a simple and intuitive model that quantitatively explains the line shape. We express the transmitted amplitude t and the reflected amplitude r as follows:

$$t=t_d+f\frac{\gamma}{i(\omega-\omega_0)+\gamma}, \tag{3}$$

$$r=r_d\pm f\frac{\gamma}{i(\omega-\omega_0)+\gamma}. \tag{4}$$

Here t_d and r_d are the direct transmission coefficients, ω_0 and γ are the center frequencies and widths of the Lorentzian from the resonance, and the factor f is the complex amplitude of the resonant mode.

The plus and minus sign in Eq. (4) corresponds to resonant modes that are even and odd, respectively, with respect to the mirror plane parallel to the slab. We note that the Lorentzian functions in Eqs. (3) and (4) correspond to the decaying amplitudes of the resonances to the reflection and transmission sides of the slab, respectively. For an even mode, the decaying amplitudes to the two sides of the slab are in phase, while for an odd mode the decaying amplitudes are 180° out of phase. Thus, the signs in Eq. (4) are different for modes with different mirror-plane symmetry properties.

The factor f can in fact be determined purely by energy conservation arguments. We note that

$$|r|^2+|t|^2=1. \tag{5}$$

Moreover, since r_d and t_d are the transmission and reflection coefficients through a uniform slab with the appropriate effective dielectric constant, we should have

$$|r_d|^2+|t_d|^2=1. \tag{6}$$

Constraints (5) and (6) together uniquely determine the factor f. Plugging Eqs. (3), (4), and (6) into Eq. (5), we have, for any ω,

$$\begin{aligned}-2|f|^2\frac{\gamma^2}{(\omega-\omega_0)^2+\gamma^2}=2|f||t_d\pm r_d|\frac{\gamma}{\sqrt{(\omega-\omega_0)^2+\gamma^2}}\\ \times\cos\left[\arg(f)-\arg(t_d\pm r_d)\right.\\ \left.-\arccos\left(\frac{\gamma}{\sqrt{(\omega-\omega_0)^2+\gamma^2}}\right)\right],\end{aligned} \tag{7}$$

which can only be satisfied if

$$f=-(t_d\pm r_d). \tag{8}$$

It is interesting to note here that the factor f is independent of the resonant linewidth γ.

The parameters r_d and t_d represent the background of the spectra. Therefore, as discussed earlier in Sec. III B, such parameters can be determined by fitting the background to the response spectra of a uniform slab, as

$$r_d=\frac{i\frac{k_{z0}^2-k_{z1}^2}{2k_{z0}k_{z1}}\sin(k_{z1}h)}{\cos(k_{z1}h)-i\frac{k_{z0}^2+k_{z1}^2}{2k_{z0}k_{z1}}\sin(k_{z1}h)}, \tag{9}$$

$$t_d=\frac{1}{\cos(k_{z1}h)-i\frac{k_{z0}^2+k_{z1}^2}{2k_{z0}k_{z1}}\sin(k_{z1}h)}, \tag{10}$$

for a plane wave with parallel wave vector k_x, incident from vacuum with a dielectric constant $\varepsilon_0=1$, through a uniform dielectric slab with a thickness h and a dielectric constant ε_1.[34] The parameters k_{z0} and k_{z1} in Eqs. (9) and (10) represent the wave vector components along the z axis in the uniform slab and are defined as

$$k_{z0}=\sqrt{\varepsilon_0\frac{\omega^2}{c^2}-k_x^2}, \tag{11}$$

$$k_{z1}=\sqrt{\varepsilon_1\frac{\omega^2}{c^2}-k_x^2}. \tag{12}$$

In obtaining Eqs. (9) and (10), we assume a positive-frequency convention, in order to be consistent with the Lorentzian functions that we have chosen for the resonance in Eqs. (3) and (4).

We note, in particular, when $t_d=1$ and $r_d=0$, from Eqs. (3), (4), and (8), the reflection and transmission coefficients become

$$t=\frac{i(\omega-\omega_0)}{i(\omega-\omega_0)+\gamma} \tag{13}$$

and

$$r=\mp\frac{\gamma}{i(\omega-\omega_0)+\gamma}. \tag{14}$$

The line shapes thus become symmetric, and the structure behaves as a narrow-band reflector with a Lorentzian reflectivity line shape. This scenario was noted previously by Wang and Magnusson.[26] In the general case when $r_d\neq 0$, on the other hand, the line shape becomes asymmetric. The transmission can vary from 0% to 100% within a very narrow frequency range. A small shift in the resonant frequency may therefore lead to a drastic change in the response function. This effect may be exploited in the design of optical switches.

We compare our theoretical predictions, as defined by Eqs. (3), (4), (8), (9), and (10), to the numerical results for the first two resonances shown in Fig. 7. (Both of these resonances are even.) The frequency ω_0 and the width γ of each resonance are determined from the simulations. The only fitting parameter here is the effective dielectric constant $\varepsilon_1(\omega)$, which we take from Eq. (2). The theoretical results thus obtained are shown as solid lines in Fig. 9. The theory agrees completely with the numerical simulations.

D. Wave vector dependence of the resonances

To explore the wave vector and polarization dependences of the resonances, we performed calculations at different values of k_x, for an incident wave that is either *s* or *p* polarized. (The *s* polarization has the electric field perpendicular to the plane of incidence, while the *p* polarization has the magnetic field perpendicular to the plane of incidence.) We determine the position and width of the resonances by Fourier transforming the decaying tail, as discussed earlier in Sec. III C. The results are summarized in Fig. 10, where we show the frequencies of the resonances as a function of k_x. Incident waves with different polarizations excite different resonances, since the two polarizations possess different symmetries with respect to the *yz*-mirror plane.

We note that, in Fig. 10, some of the bands do not continue to the Γ point. In other words, certain resonances at Γ do not couple to either polarization of the incident wave. A closer examination of Fig. 10 reveals that all these uncoupled resonances are singly degenerate. Previously, this effect was observed experimentally by Pacradoni *et al.*[14] and discussed theoretically by Paddon and Young[13] and Ochiai and Sakoda.[25]

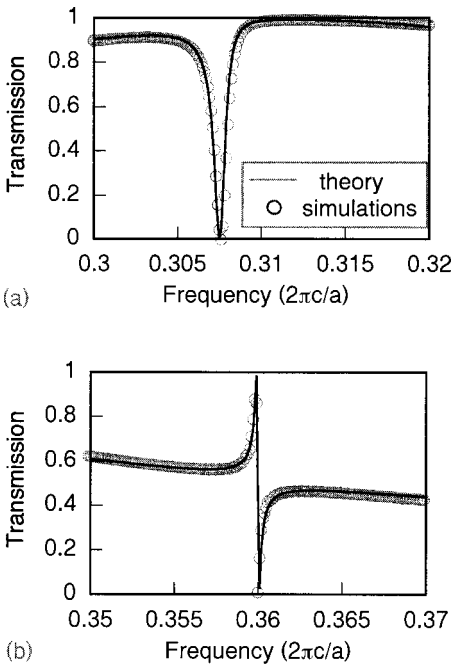

FIG. 9. Comparison of theory and simulations. The empty circles in (a) and (b) are numerical results taken from Fig. 7(a), which corresponds to the two lowest-frequency resonances. The solid lines are theoretical predictions from Eqs. (3), (8), (9), and (10). The parameters of the theory for the two resonances are (a) $\omega_0=0.3076\times 2\pi c/a$, $\gamma=4.191\times 10^{-4}\times 2\pi c/a$ and (b) $\omega_0=0.3601\times 2\pi c/a$, $\gamma=7.2483\times 10^{-5}\times 2\pi c/a$.

To further explore the wave vector dependence of the resonance, in Fig. 11 we plot the quality factors of the resonances as a function of k_x for the four lowest bands in Fig. 10. For bands with different symmetry properties, the behaviors of the quality factors are very different. The *Q* factors

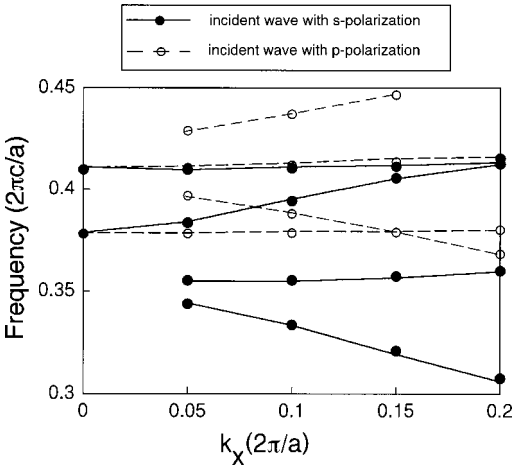

FIG. 10. Frequencies of the resonances as a function of k_x for the structure as shown in Fig. 1 as determined from the time-domain simulations. The solid circles correspond to the resonances that are excited by the *p*-polarized incident wave: the open circles correspond to the resonances that are excited by the *s*-polarized incident waves. Notice that some of the bands do not continue to $k_x=0$, indicating the existence of uncoupled states at Γ.

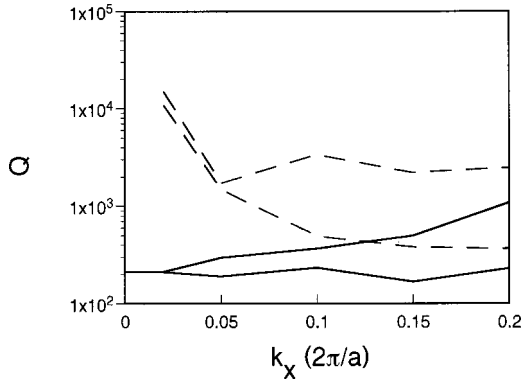

FIG. 11. Quality factor as a function of k_x for the four lowest bands in Fig. 10. The solid lines correspond to modes that connect to the doubly degenerate state at the Γ point. The dashed lines correspond to modes that connect to the singly degenerate state at the Γ point.

approach a constant as k_x vanishes for the modes that connect to the doubly degenerate states at Γ. For the modes that connect to the singly degenerate states, on the other hand, the Q factors of the modes diverge. The calculation clearly demonstrates that the symmetry of the modes can significantly influence the photon lifetime of the resonances.

E. Radius dependence of the resonance

In addition to symmetry-related effects, the lifetime of the resonances is also strongly influenced by the radius of the holes. At the limit where the radius of the holes approaches zero, the Q factor for all the resonances should diverge, since the resonances asymptotically become true guided modes. To demonstrate this effect, we plot in Fig. 12 the transmission spectra at normal incidence for four different structures with the radius varying from $0.05a$ to $0.20a$. The spectral feature for the resonances indeed becomes sharper as the radius becomes smaller. For the lowest-order resonances, the Q factor varies from approximately 5000 at $r=0.05a$, to 213 at $r=0.20a$. At a larger radius, the Q factor should be even lower.

The tunability of the quality factor with respect to the radius of the holes is important for light-emitting diode (LED) and laser applications. For photonic-crystal resonant-cavity LED structures, optimal efficiency occurs when the linewidth of the resonances become comparable to the linewidth of the emitter.[35] On the other hand, for a laser structure, a high-Q resonance is typically desirable for threshold reduction. Therefore, as we have demonstrated in this paper, photonic crystal slab structures are very versatile and can be specifically tailored for different light-emitting applications.

IV. SUMMARY

In summary, we present a three-dimensional frequency and time-domain analysis of resonances in photonic crystal slab structures. These resonances are strongly confined with the dielectric slab and yet at the same time are coupled to radiation modes. For external light incident upon these slabs, the transmission and reflection spectra are strongly modified by the presence of these resonances. The line shapes exhibit complex asymmetric characteristics. We show that all the complexities in the line shapes can be accounted for with a simple analytic model describing the interference between direct transmission (or reflection) and the exponential decaying amplitudes of the resonances. We also demonstrate that the quality factor of these resonances is strongly influenced by the symmetry of the modes and the radius of the holes.

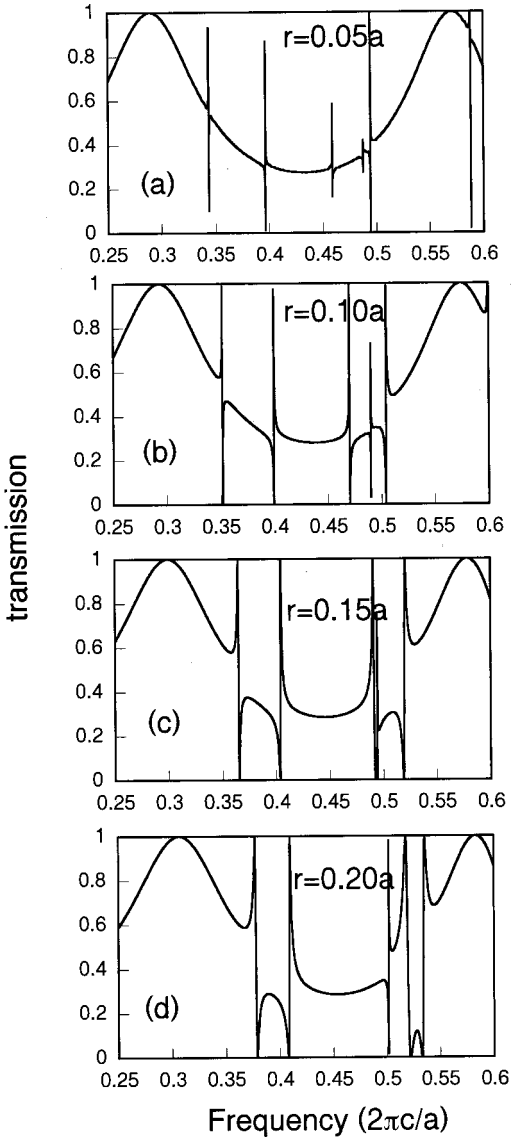

FIG. 12. Transmission spectra at normal incidence for crystal slab structures with a radius of (a) $0.05a$, (b) $0.10a$, (c) $0.15a$, and (d) $0.20a$. All structures have a thickness of $0.5a$ and a dielectric constant of 12.

ACKNOWLEDGMENT

This work was supported in part by the Material Research Science and Engineering Center program of the National Science Foundation under Award No. DMR-9400334.

[1] S. Fan, P. R. Villeneuve, J. D. Joannopoulos, and E. F. Schubert, Phys. Rev. Lett. **78**, 3294 (1997).
[2] S. G. Johnson, S. Fan, P. R. Villeneuve, J. D. Joannopoulos, and L. A. Kolodzjeski, Phys. Rev. B **60**, 5751 (1999).
[3] O. Painter, T. Vuckovic, and A. Scherer, J. Opt. Soc. Am. B **16**, 275 (1999).
[4] T. Baba, N. Fukaya, and J. Yonekura, Electron. Lett. **35**, 654 (1999).
[5] S. Kuchinsky, D. C. Allan, N. F. Borrelli, and J.-C. Cotteverte, Opt. Commun. **175**, 147 (2000).
[6] S. Y. Lin, E. Chow, S. G. Johnson, and J. D. Joannopoulos, Opt. Lett. **25**, 1297 (2000).
[7] H. Benisty *et al.*, Appl. Phys. Lett. **76**, 532 (2000).
[8] A. Chutinan and S. Noda, Phys. Rev. B **62**, 4488 (2000).
[9] M. Kanskar, P. Paddon, V. Pacradouni, R. Morin, A. Busch, J. F. Young, S. R. Johnson, J. MacKenzie, and T. Tiedje, Appl. Phys. Lett. **70**, 1438 (1997).
[10] P. R. Villeneuve, S. Fan, S. G. Johnson, and J. D. Joannopoulos, IEE Proc.-J: Optoelectron. **145**, 384 (1998).
[11] M. Boroditsky, R. Vrijen, T. F. Krauss, R. Coccioli, R. Bhat, and E. Yablonovitch, J. Lightwave Technol. **17**, 2096 (1999).
[12] V. N. Astratov, I. S. Chushaw, R. M. Stevenson, D. M. Whittaker, M. S. Skolnick, T. F. Krauss, and R. M. De la Rue, J. Lightwave Technol. **17**, 2050 (1999).
[13] P. Paddon and J. F. Young, Phys. Rev. B **61**, 2090 (2000).
[14] V. Pacardoni, W. J. Mandeville, A. R. Crown, P. Paddon, J. F. Young, and S. R. Johnson, Phys. Rev. B **62**, 4204 (2000).
[15] A. R. Cowan, P. Paddon, V. Pacradouni, and J. F. Young, J. Opt. Soc. Am. A **18**, 1160 (2001).
[16] A. A. Erchak, D. J. Ripin, S. Fan, J. D. Joannopoulos, E. P. Ippen, G. S. Petrich, and L. A. Kolodzjeski, Appl. Phys. Lett. **78**, 563 (2001).
[17] M. Meier, A. Mekis, A. Dodabalapur, A. Timko, R. E. Slusher, and J. D. Joannopoulos, Appl. Phys. Lett. **74**, 7 (1999).
[18] M. Imada, S. Noda, A. Chutinan, T. Tokuda, M. Murata, and G. Sasaki, Appl. Phys. Lett. **75**, 316 (1999).
[19] A. Mekis, A. Dodabalapur, R. E. Slusher, and J. D. Joannopoulos, Opt. Lett. **25**, 942 (2000).
[20] S. Peng and G. M. Morris, J. Opt. Soc. Am. A **13**, 993 (1996).
[21] J. D. Joannopoulos, R. D. Meade, and J. N. Winn, *Photonic Crystals: Molding the flow of light* (Princeton University Press, Princeton, 1995).
[22] For a review on finite-difference time-domain methods, see K. S. Kunz and R. J. Luebbers, *The Finite Difference Time Domain Methods for Electromagnetics* (CRC Press, Boca Raton, 1993); A. Taflove and S. C. Hagness, *Computational Electrodynamics: The finite-difference time-domain method* (Artech House, Boston, 2000).
[23] J. P. Berenger, J. Comput. Phys. **114**, 185 (1994).
[24] S. S. Wang and R. Magnusson, Appl. Phys. Lett. **61**, 1022 (1992).
[25] T. Ochiai and K. Sakoda, Phys. Rev. B **63**, 125107 (2001).
[26] S. S. Wang and R. Magnusson, Opt. Lett. **19**, 919 (1994).
[27] A. Sharon, D. Rosenblatt, and A. A. Friesem, Opt. Lett. **21**, 1564 (1996).
[28] T. Tamir and S. Zhang, J. Opt. Soc. Am. A **14**, 1607 (1997).
[29] S. M. Norton, T. Erdogan, and G. M. Morris, J. Opt. Soc. Am. A **14**, 629 (1997).
[30] S. M. Norton, G. M. Morris, and T. Erdogan, J. Opt. Soc. Am. A **15**, 464 (1998).
[31] G. Levy-Yurista and A. A. Friesem, Appl. Phys. Lett. **77**, 1596 (2000).
[32] U. Fano, Phys. Rev. **124**, 1866 (1961).
[33] R. V. Andaloro, H. J. Simon, and R. T. Deck, Appl. Opt. **33**, 6340 (1994).
[34] P. Yeh, *Optical Waves in Layered Media* (Wiley, New York, 1988).
[35] S. Fan, P. R. Villeneuve, and J. D. Joannopoulos, IEEE J. Quantum Electron. **36**, 1123 (2000).